

Strain-Driven Surface Reactivity in Magnesium-Ion Battery Cathodes

Jae Jin Kim,* Bilash KC, Haesun Park, Aditya Sundar, Guennadi Evmenenko, D. Bruce Buchholz, Jinglong Guo, Brian J. Ingram, Peter Zapol, Robert F. Klie, and Timothy T. Fister*



Cite This: *Chem. Mater.* 2024, 36, 1342–1351



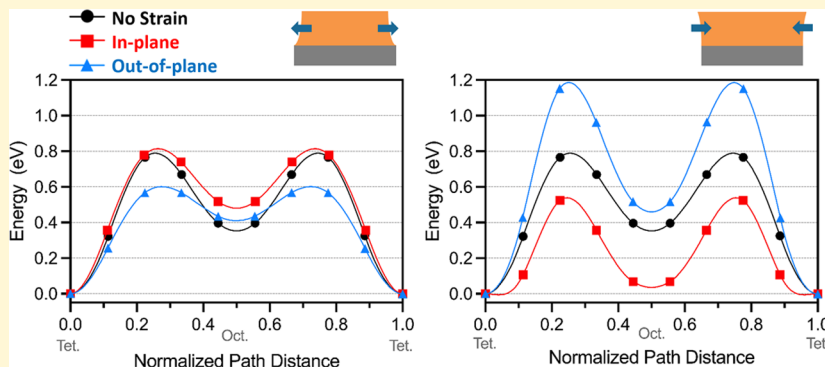
Read Online

ACCESS |

Metrics & More

Article Recommendations

Supporting Information



ABSTRACT: Successful deployment of a Mg-ion battery requires cathodes that can achieve reversible Mg intercalation and high energy density. Recent theoretical and experimental studies indicated that the overall transport is likely limited by sluggish Mg transport at the cathode–electrolyte interface and not Mg diffusion through bulk. In this work, we investigated the surface electrochemical activity of Mg ions by using a spinel-structured manganese oxide thin-film model system and in situ X-ray scattering. In combination with post-mortem microscopy analysis, we found that magnesium insertion was more favorable than subsequent extraction near the surface of the $\text{Mg}_x\text{Mn}_2\text{O}_4$ film, resulting in overmagnesiation, and eventually amorphization of the surface. This structural irreversibility and high overpotential required for Mg extraction could explain significant voltage hysteresis and Mg surface enrichment previously observed in bulk cathodes. Density functional theory calculations suggested that the tendency for the Mg surface enrichment could be associated with Mg diffusion kinetics, which varies with the strain state evolved due to constrained film volume change during Mg insertion and extraction. Particularly, out-of-plane Mg migration was predicted to be favorable in the tensile strain rather than in the compressive case.

INTRODUCTION

Multivalent rechargeable batteries have often been considered a natural successor to current lithium ion technology. In principle, replacing Li^+ with a divalent ion (e.g., Mg^{2+} , Ca^{2+} , and Zn^{2+}) could enable the use of a dendrite-free metal anode and potentially double the specific capacity of the cathode.¹ The natural abundance of multivalent elements in Earth's crust is an additional merit, potentially lowering material costs. While there has been steady progress discovering new electrolytes capable of reversible plating and stripping of Mg and Ca on the anode side,^{1–4} the most successful cathodes—in terms of capacity and reversibility—have been in lower voltage systems, like the original magnesium Chevrel phase Mo_6S_8 ^{5,6} and more recent efforts on layered-TiS₂/⁷thiospinel.⁸ In a large part, this is due to the lack of multivalent electrolytes with sufficient stability over several volts.^{9,10} However, even with an anodically stable electrolyte, magnesium cathodes still suffer from either low energy density or inferior rate performance with significant hysteresis.^{11–13} These limitations have typically been assumed to be due to poor bulk Mg-ion mobility in a

crystal lattice. However, theoretical calculations¹⁴ and recent nuclear magnetic resonance (NMR) studies¹⁵ on oxide spinels show that bulk Mg-ion mobility is in fact quite high. In that sense, the overall transport is likely bottlenecked by a mechanism at the cathode–electrolyte interface. For instance, magnesium-based spinel oxides are reported to be susceptible to surface Mg enrichment.¹⁶ In particular, MgMn_2O_4 is often prone to site inversion due to competition between Mg and Mn for the octahedral site, unlike LiMn_2O_4 (LMO) where Li predominantly occupies the tetrahedral site. This cation exchange, accompanied by excess Mg, is considered to cause the formation of a rock-salt-like surface layer at MgMn_2O_4 , which could impede Mg insertion/extraction.^{17–19} Similarly,

Received: September 29, 2023

Revised: January 2, 2024

Accepted: January 3, 2024

Published: January 18, 2024



recent data on MgMnCrO_4 showed that during charge or deep discharge, Mg migrates from the tetrahedral site to the open 16c octahedral site, resembling a cation-ordered rock-salt.²⁰

In this study, we investigated the electrochemical activity (i.e., insertion and extraction) of magnesium ion near the surface of the manganese-based spinel structure, $\text{Mg}_x\text{Mn}_2\text{O}_4$ (MMO), which has been suggested as a promising multivalent cathode based on first-principles calculation in consideration of thermodynamic stability of charged/discharged states and intercalating ion mobility.¹⁴ Unlike previous bulk studies, we used a model thin-film electrode to better model the electrode–electrolyte interface, taking advantage of its well-controlled surface morphology and crystallographic orientation.^{21,22} By electrochemically ion-exchanging lithium for magnesium in a 10-nm-thick LMO film,^{23,24} real-time X-ray surface scattering revealed that magnesium insertion was inherently more favorable than subsequent extraction and that the charged Mn_2O_4 cathode was actually unstable at open circuit. The tendency for the surface of the MMO film to be overmagnesiated during discharge also led to pronounced structural irreversibility that can contribute to overpotentials during subsequent cycling. Based on a combination of operando characterization and density functional theory (DFT) calculations, it is suggested that the inherent strain developed in a thin film, or even the surface region of a bulk cathode, could be a driving mechanism for this hysteresis and may have negative consequence for the stability of a charged cathode, even under open-circuit conditions.

■ EXPERIMENTAL METHODS AND COMPUTATIONAL DETAILS

Sample Fabrication and Characterization. High-quality (111)-oriented LiMn_2O_4 (LMO) thin films were grown by pulsed laser deposition (nanoPLD 1000 with 248 nm KrF excimer laser, PVD Products) on (111) SrTiO_3 (STO) substrates ($10 \times 3 \text{ mm}^2$) with a conducting SrRuO_3 (SRO) interlayer used as a current collector. As seen in the inset of Figure 1, the LMO film was masked to $4 \times 3 \text{ mm}^2$ with exposed SRO side tabs for electrical contact. Ex situ specular X-ray reflectivity and diffraction were performed with

Rigaku ATXG diffractometer equipped with an 18 kW Cu rotating anode ($\lambda = 1.5418 \text{ \AA}$) and a collimated beam of $0.1 \times 2.0 \text{ mm}^2$. High-resolution measurements of LMO peaks were achieved using a Ge (220) two-bounce monochromator ($\lambda = 1.5406 \text{ \AA}$). Off-specular phi scans were performed with a Smartlab Gen 2 diffractometer equipped with a 9 kW Cu rotating anode ($\lambda = 1.5418 \text{ \AA}$) and chi circle using a collimated beam of $0.05 \times 2.00 \text{ mm}^2$ and two 0.5° soler slits. Thin-film X-ray diffraction (XRD) showed that the films were highly textured and oriented in-plane with the STO substrate but that the lattice constants were relaxed to the bulk values of the spinel due to the mismatch in lattice constants (~5% in-plane). Detailed description of the film growth and characterization can be found elsewhere.^{25,26}

Electrochemical and In Situ X-ray Reflectivity Measurements. The LMO films were cycled in 0.05 M $\text{Mg}[\text{TPFA}]_2$ (TPFA = tetrakis(perfluoro-*tert*-butoxy)aluminate) in diglyme, which has previously been shown to be anodically stable to ~5.4 V vs Mg/Mg²⁺,²⁷ using an X-ray-compatible cell analogous to a beaker cell. A capacitive copper wire counter electrode and a leakless Ag/AgCl reference electrode (eDAQ, Inc.) were used for the measurement. Additional attempts to use a Mg counter/reference consistently resulted in lower open-circuit and operating voltages than those expected for this cathode, possibly due to the chemical instability of Mg with the electrolyte. Subsequent potentials in this study are shifted to the Mg/Mg²⁺ redox couple for comparison with previous literature data on magnesium batteries. In situ X-ray reflectivity (XRR) measurements were performed at the Advanced Photon Source, sector 33BM, using 21 keV X-rays focused to $2 \times 0.2 \text{ mm}^2$. The operando scattering focused on features along the specular (111) crystal truncation rod. As seen in Figure 1, we primarily focused on the low-angle XRR and the higher-angle regions near the 111 and 222 spinel thin-film Bragg peaks. The Bragg peaks were used to evaluate the composition and crystal structure of the film, while the XRR provided an independent measure of the average density and overall thickness of each layer. Each region required a 5–10 min scan in X-ray momentum transfer (q). For the operando scattering, films were first charged (delithiation) and then discharged (magnesiation) using cyclic voltammetry at 0.2 mV/s of scan rate. The films were held at 3.8 V until the spinel peaks reached an asymptotic d -spacing consistent with the complete removal of lithium to the $\lambda\text{-Mn}_2\text{O}_4$ phase. Films were then discharged to 1.3 V, similar to previous galvanostatic cycling limits used for bulk magnesium spinel cathodes.²⁸

Transmission Electron Microscopy Characterization. High-resolution structural characterization was performed in an aberration-corrected scanning transmission electron microscope (STEM, JEOL ARM200CF). The instrument is equipped with a cold-field-emission electron source operated at 200 kV, as well as a high-angle annular dark-field (HAADF) detector, an Oxford-XMAX100TLE energy dispersive X-ray spectrometer (EDXS), and a postcolumn Gatan Continuum imaging filter for electron energy-loss spectroscopy (EELS). Using a convergence semiangle of 28 mrad, a spatial resolution of 73 pm for imaging and spectrum imaging and an energy resolution of 350 meV can be achieved. The thin-film sample was prepared in a cross-sectional sample geometry using conventional focused ion-beam milling and a lift-out procedure. HAADF images were acquired using collection angles from 90 to 174.5 mrad. EELS measurements were performed using a probe semiconvergence angle of 17.8 mrad and a 53.4 collection angle.

Computational Details. Density functional theory (DFT) calculations²⁹ were performed as implemented in the Vienna ab initio simulations package (VASP)³⁰ for the evaluation of Mg migration in the $\lambda\text{-Mn}_2\text{O}_4$ spinel framework. The nudged-elastic-band (NEB) method³¹ was used to calculate the Mg migration barrier. The core electrons were described by the projector-augmented wave (PAW) potentials,^{32,33} and the plane-wave basis sets with a cutoff energy of 520 eV were adopted for the description of valence electrons. The exchange-correlation functional in the Kohn–Sham equation suggested by Perdew–Burke–Ernzerhof (PBE) was used.³⁴ The simulation cell was generated by multiplying lattice vectors

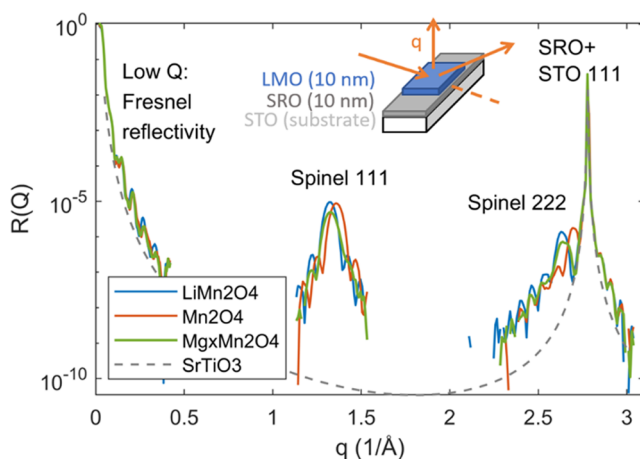


Figure 1. Overview of X-ray reflectivity $R(Q)$ at the low-angle and crystal truncation rod regimes with data taken at the start (blue), fully delithiated (orange), and partially magnesiated (2.5 V; green). q is the X-ray momentum transfer. The calculated crystal truncation rod for the (111) SrTiO_3 (STO) substrate (gray dotted) is also shown for reference. Inset: diagram of the thin-film heterostructure and scattering geometry.

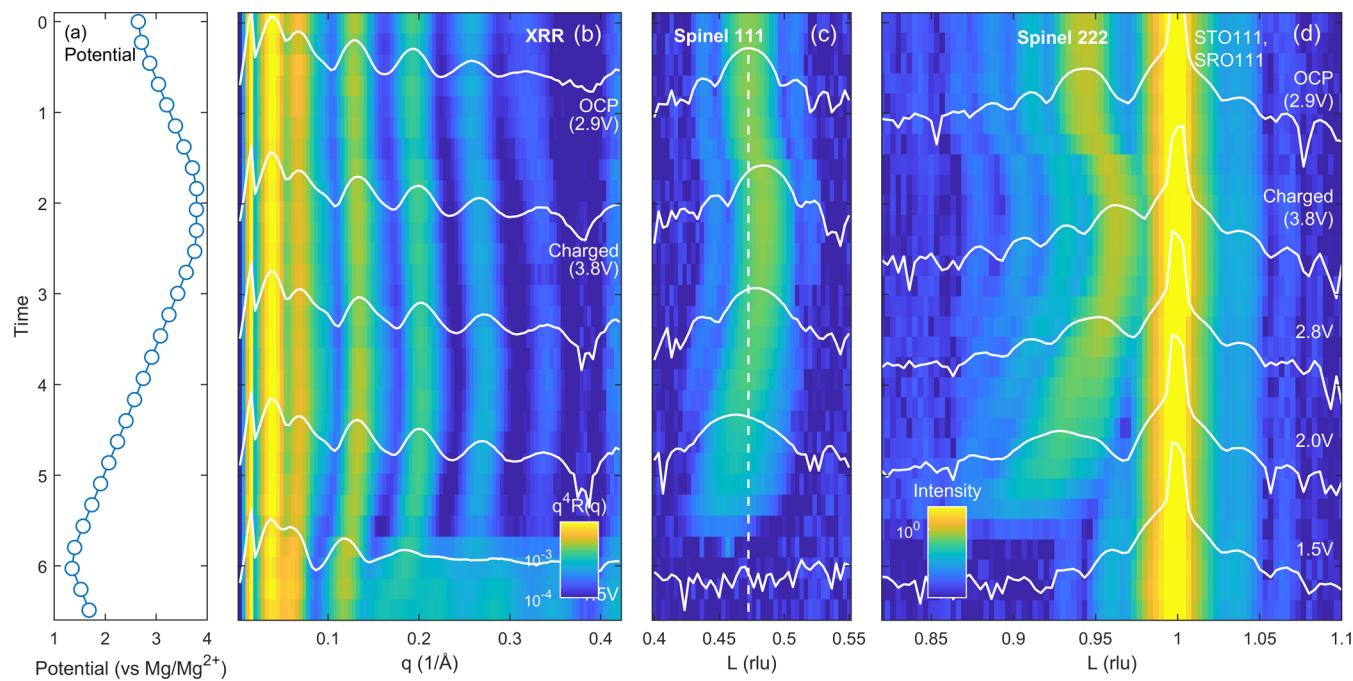


Figure 2. (a) Plot of the electrical potential applied during the X-ray scattering measurement. Waterfall plots of the surface scattering measured at (b) low- q X-ray reflectivity (XRR), (c) spinel 111, and (d) spinel 222 peaks. The Fresnel-regime reflectivity is scaled by q^4 . Selected scattering intensity curves are overlaid. The vertical dashed line in panel (c) is the initial 111 peak position for reference. Note that the color scale is logarithmic in each case due to the measurement's large dynamic range.

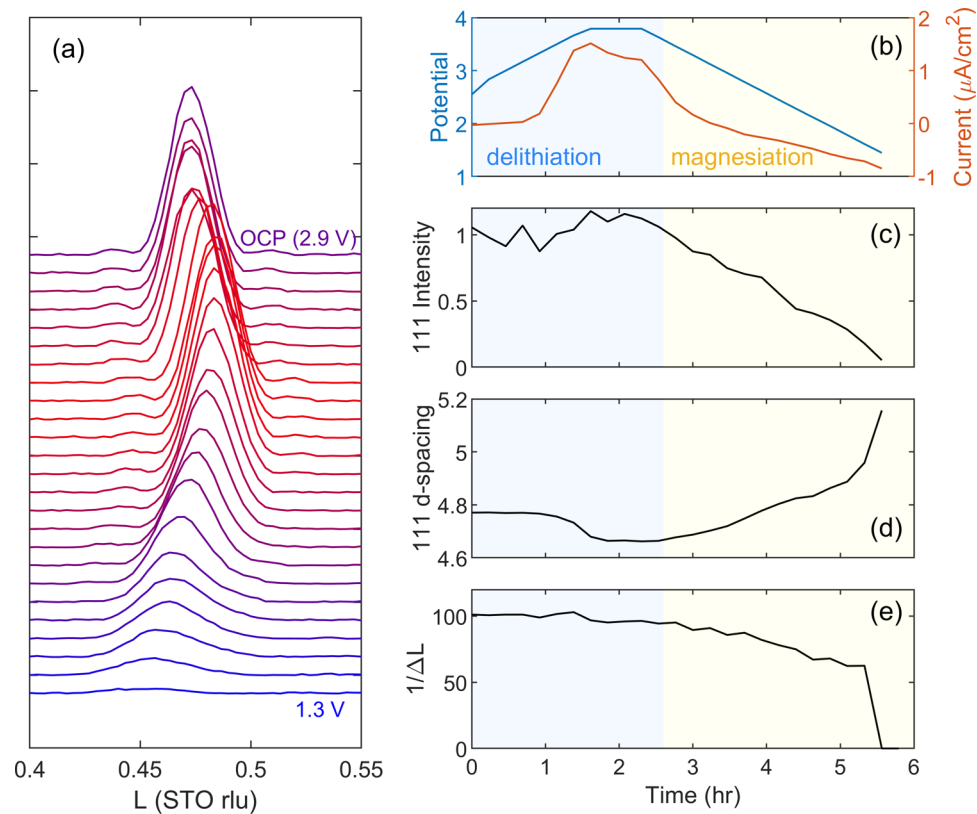


Figure 3. (a) Spinel 111 peak during delithiation and subsequent magnesiation. The y-axis is scattering intensity in a linear scale. Curves are offset vertically with the starting peak at the open-circuit potential (OCP) at the top. The color scale reflects the voltage range of cyclic voltammetry (CV) between 1.3 (blue) and 3.8 V (red). (b) Voltage and current density during CV, which can be compared to (c) integrated intensity, (d) 111 d -spacing, and (e) inverse full width at half-maximum (i.e., crystalline thickness) measured from the 111 peak as a function of time. The background colors in panels (b)–(e) are used to denote regions of delithiation and magnesiation.

($[0\bar{1}0]$, $[0\bar{1}\bar{1}]$, and $[1\bar{1}\bar{1}]$) to construct a hexagonal simulation cell where the a , b , and c axes correspond to $(1\bar{1}0)$, $(0\bar{1}1)$, and $(1\bar{1}\bar{1})$ directions in the cubic spinel cell. The biaxial strain, ϵ , was applied along the a and b directions of the simulation cell. The strain was applied with respect to the lattice parameter of cubic spinel LMO and thus the a and b lattice parameters of the simulation cell were strained by $\sqrt{2}\epsilon$. To maintain the biaxially strained structure during the structural relaxation, only the normal stress in the c direction and shear stress were included during the cell relaxation.

RESULTS AND DISCUSSION

As seen in Figure 2, both the low-angle X-ray reflectivity (XRR) and the higher-angle regions near the 111 and 222 film Bragg peaks show significant changes during voltammetry, which are amplified at higher q (also shown as L , the reciprocal lattice unit for SrTiO₃ (STO), $q = 2\pi L/d_{\text{STO},111}$). The linearly changing potential is shown in Figure 2a for reference. During the initial charging sweep and hold at 3.8 V, shifts in the spinel Bragg peaks (Figure 2c,d) showed a contraction of the out-of-plane lattice constant, consistent with known lattice shifts of LMO during delithiation.²⁵ On the other hand, the low-angle XRR (Figure 2b) showed a small amount of change associated with the reduction in thickness of the spinel layer from this lattice contraction. During the subsequent discharge scan, the interference fringes in the XRR and the spinel Bragg peaks shifted back to lower q /lower L , consistent with magnesium-ion insertion. In the meantime, the amplitude of the spinel peaks was reduced (as seen in Figure 1) due to the reduced form factor of the (111) and (222) Bragg conditions with Mg-ion substitution (discussed in detail in the following section). This is contrary to largely unchanged peak intensity observed when one lithium is inserted into a λ -Mn₂O₄ spinel thin film.²⁵ Note that the SrRuO₃ (SRO) and STO peaks were unaffected by any of the potential conditions used in this study.

Following previous bulk protocols,²⁸ the thin-film spinel electrode was discharged beyond its open-circuit potential (OCP, ~2.9 V), eventually reaching to 1.3 V vs Mg/Mg²⁺. Approaching this deep-discharge condition, the spinel Bragg peaks began to broaden and abruptly lost intensity near 1.3 V. This coincided with a shift in momentum transfer beyond the original d -spacing of the LMO film, occurring at ~2.5 V, indicating an expansion of the crystal lattice with increasing Mg-ion insertion. Despite the absence of spinel diffraction peaks at 1.3 V, the XRR continued to show bilayer reflectivity with an abrupt shift that implied a sharp increase in the overall thickness and interfacial roughness when deeply discharged.

To understand the crystallographic changes in the spinel film, the 111 diffraction peak, located in the midzone of the overall crystal truncation rod, can be further examined. At this position, its overall diffraction intensity is purely from the cathode thin film, unlike the region near the 222 peak where both contributions from the underlying SRO interlayer peak and STO substrate's crystal truncation rod are substantial. The 111 peak is plotted in Figure 3a in linear scale. Figure 3b shows the potential and current during cyclic voltammetry (CV), which can be compared to the integrated intensity of the peak, its d -spacing (from the peak center), and its “crystalline thickness” (given by its inverse full width at half-maximum in L , analogous to Scherrer broadening in powder diffraction), plotted in Figure 3c–e, respectively. Note that any type of gradient in magnesiation through the depth of the film would also broaden the film Bragg peak in a similar manner. However, for simplicity, the thickness of the crystalline portion was calculated assuming no concentration gradient. The

potential regions corresponding to delithiation and magnesiation are labeled and colored for reference. During delithiation (i.e., charging), the 111 peak showed largely unchanged overall intensity, but noticeably shifted to higher L , reflecting the contraction of the lattice to $d_{111} = 4.66 \text{ \AA}$, which would correspond to a spinel lattice constant of 8.07 \AA , close to the value for λ -Mn₂O₄ cubic spinel (8.029 \AA).³⁵ During the cathodic sweep, there was a steady decrease in the integrated peak intensity and a shift to larger d -spacing (i.e., lower L), reflecting the expansion of the crystal lattice during magnesiation. The reduction in intensity was, at first, largely due to the decrease in the spinel 111 structure factor with Mg occupancy (see Figure S1). At deep discharge, the Bragg peak noticeably broadened and shifted to a further lower L , suggesting that the crystalline portion of the film was shrinking in thickness, even though the unit cell rapidly expanded up to $d_{111} = \sim 5.18 \text{ \AA}$.

On the other hand, while the spinel Bragg peaks eventually disappeared at deep discharge, the interference fringes in the XRR continued to shift to lower q , indicating an overall expansion of the film, even as the crystalline portion was shrinking (Figure 4 and its inset). This suggested that, at deep

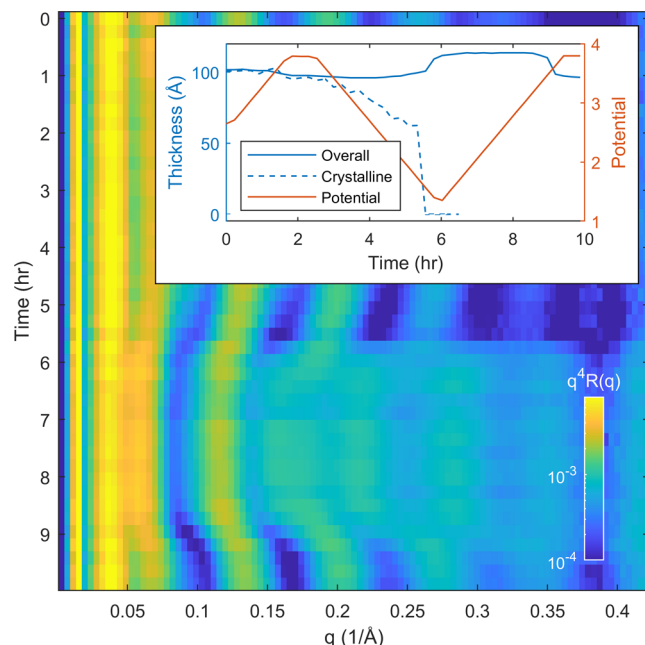


Figure 4. Waterfall plot of low- q X-ray reflectivity, extended from Figure 2b, during initial delithiation and subsequent magnesiation and demagnesiation. Inset plot shows the overall thickness overlaid with the thickness of the crystalline portion of the film.

discharge, the substantial change in lattice constant (~10%) eventually amorphized the spinel thin film or eliminated its epitaxial relationship to the substrate (i.e., became a powder). The integrated current passed during discharge, normalized to the volume of the Mn₂O₄ charged electrode, was equivalent reaching toward Mg₂Mn₂O₄, far beyond the intended spinel composition MgMn₂O₄. Here, it is assumed that all of the cathodic current is consumed for the magnesiation of the thin film. This overmagnesiated phase was closer in composition to a mixture of the binary MgO and MnO rock-salt phases and evidently lost the single-crystal nature of the initial electrode. Interestingly, during continued charging scan, the Kiessig

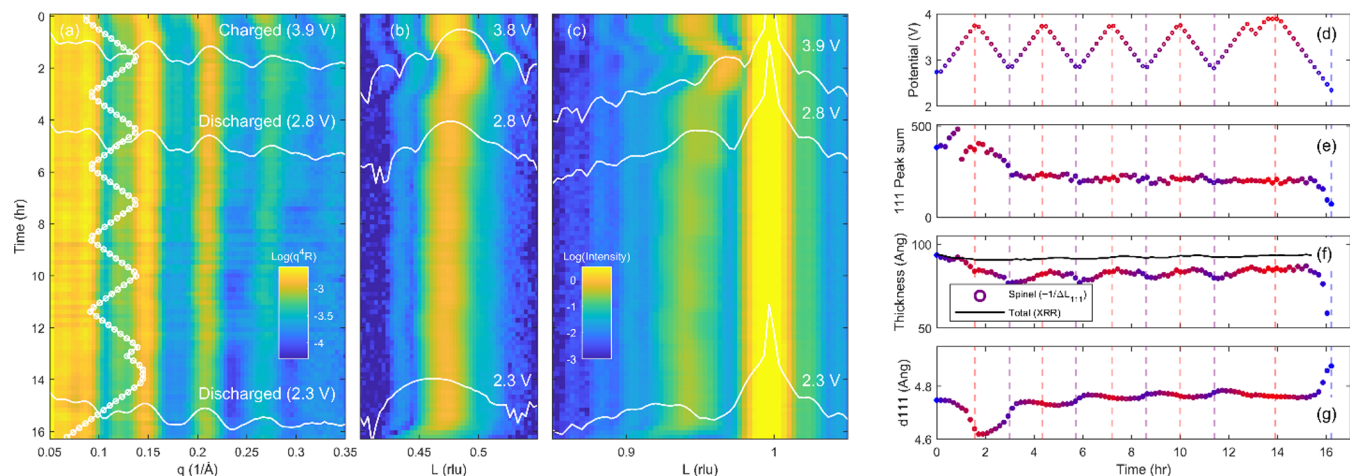


Figure 5. Similar to Figure 2, waterfall plots of the crystal truncation rod in (a) low- q X-ray reflectivity (XRR) regime and (b) near 111 spinel, and (c) 222 spinel peaks. The potential range is overlaid in panel (a). Select curves from 3.9 V (delithiated), 2.8 V (magnesiated), and the final deep discharge (2.3 V) are shown in each case. (d) Potential at each point as a function of time. Using the 111 peak, the (e) integrated intensity, (f) spinel thickness, and (g) d -spacing are plotted. The overall film thickness (black solid line), extracted from the low- q XRR, is overlaid in panel (f). Dashed lines at times corresponding to the potential end points of the cyclic voltammetry are overlaid (d–g) for comparison.

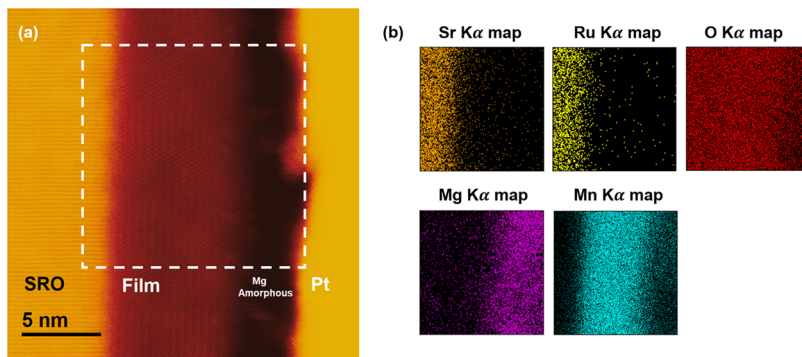


Figure 6. (a) Atomic-resolution high-angle annular dark-field (HAADF) image showing the thickness of crystalline and Mg-rich amorphous portions of the $Mg_xMn_2O_4$ film along its [112] crystal orientation, after being discharged to 2.3 V vs Mg/Mg²⁺ during operando X-ray scattering measurements. (b) Energy dispersive spectroscopy (EDS) map from the region within the white dotted square shown in panel (a), showing the distribution of Sr, Ru, O, Mg, and Mn from the interface with the conductive SrRuO₃ (SRO) buffer layer to the surface of the $Mg_xMn_2O_4$ film.

fringes from the thin film shifted back to higher q at ~ 3.6 V, indicating a reversible contraction of the lattice, coinciding with an oxidizing current corresponding to demagnesiation and electrolyte decomposition. While this result suggested that the overmagnesiated spinel cathode might be still active and electrochemically reversible, the >2 V overpotential to remove Mg was impractically large, albeit similar to the previous full cell data with the Mn–Cr-based spinel cathode.¹⁹

Based on these first studies, a second sample was tested over a more limited potential range, 2.8–3.8 V, to see if magnesium intercalation was more reversible at shallower discharge conditions. Scattering data and analysis of the 111 spinel peak from this sample are shown in Figure 5 in a similar manner to Figures 2–4. Change in current density during CV measurements is provided in Figure S2. The initial ion exchange during the first cycle's charge and discharge sweeps was nearly identical to changes seen between 2.8 and 3.8 V in the first sample. However, subsequent cycling of the magnesiated cathode showed nearly no change in the strength of the 111 peak, indicating limited Mg insertion and extraction. It was consistent with small changes in the 111 d -spacing (Figure 5b,g). While the lattice constant did not contract to the open λ -Mn₂O₄ spinel conditions achieved during the first

cycle's delithiation, there were measurable shifts ($\sim 0.8\%$) of d -spacing during subsequent cycling, indicating limited reversibility. In accordance with the first film (see Figure 3e for the first ~ 5 h), as shown in Figure 5f, the thickness of the crystalline spinel portion of the film (open circles) appeared to shrink during discharge, while the overall film thickness (solid line) remained roughly constant from the low- q XRR measurement. Like the first film, this could suggest that a portion of the film, presumably near the surface, formed a magnesium-rich nonspinel component, which was not registered to the 111 orientation of the underlying films and substrate. Unlike the first film cycled to deep discharge, however, the crystalline portion of the film partially increased back at high potential, suggesting that the overmagnesiated surface region can be still demagnesiated to some degree. However, this surface layer—which was potentially amorphized—could be a barrier for through-plane Mg transport.

As a final comparison with the first sample, the second sample was discharged to 2.3 V to see if it could be magnesiated further. During this deep-discharge process, the 111 and 222 peaks shifted and broadened far beyond the previous low cutoff voltage (2.8 V), consistent with the behavior of the first sample. After reaching 2.3 V, the

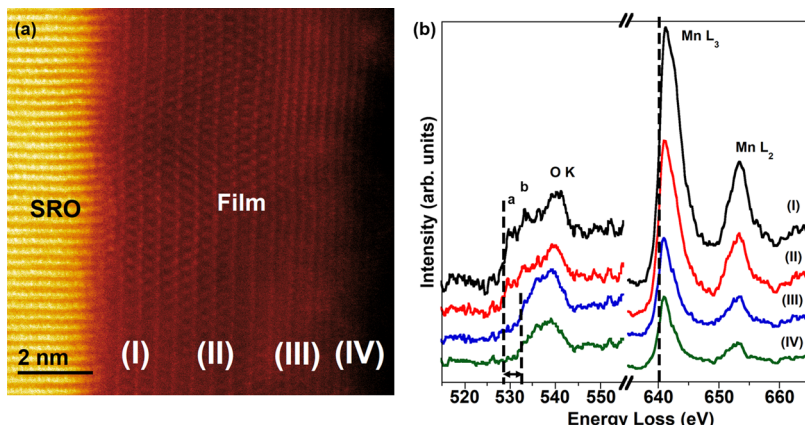


Figure 7. (a) Atomic-resolution high-angle annular dark-field (HAADF) image of the $\text{Mg}_x\text{Mn}_2\text{O}_4/\text{SrRuO}_3$ (SRO) region along the [112] $\text{Mg}_x\text{Mn}_2\text{O}_4$ orientation, after being discharged to 2.3 V vs Mg/Mg^{2+} during operando X-ray scattering measurements. Four distinct regions with different crystal structures in the $\text{Mg}_x\text{Mn}_2\text{O}_4$ film are labeled from I to IV. The corresponding electron energy-loss spectroscopy data for each region are displayed in panel (b), showing the O K- and Mn L-edges; the dashed lines at 529 and 532 eV indicate the shift in the O K-edge onset from region I to IV, respectively.

voltammetry was stopped, and the sample was removed for *ex situ* transmission electron microscopy (TEM) characterization. Figures 6 and 7 show atomic-resolution high-angle annular dark-field (HAADF) images of the $\text{Mg}_x\text{Mn}_2\text{O}_4/\text{SRO}$ region along the film's [112] crystal orientation. The atomically sharp and epitaxial interfaces between the SRO and STO were confirmed (see Figure S3), and the $\text{Mg}_x\text{Mn}_2\text{O}_4$ film was found to maintain an epitaxial relationship with the SRO buffer layer after operando X-ray scattering measurements. Lower-magnification images indicated that the average surface roughness of the $\text{Mg}_x\text{Mn}_2\text{O}_4$ film was 1–2 nm after deep discharge. As shown in Figure 6a, the crystallinity of the $\text{Mg}_x\text{Mn}_2\text{O}_4$ film was preserved within the first ~6 to 7 nm from the interface with the conductive SRO buffer layer, while an amorphous layer was formed near the film surface. Note that, as can be seen in Figure 5f, after deep discharge, the thickness of the crystalline portion observed by TEM was similar to the “spinel thickness (~6 nm)” calculated from thin-film Bragg peak analysis, while the overall thickness, including the noncrystalline region, was similar to the thickness (~9.6 nm) measured by the low-*q* XRR. Figure 6b shows energy dispersive spectroscopy (EDS) mapping within the white dotted square region displayed in Figure 6a. Quantitative compositional analysis indicated that, along the film thickness up to ~4 to 5 nm from the $\text{Mg}_x\text{Mn}_2\text{O}_4/\text{SRO}$ interface, the Mg/Mn atomic ratio was ~0.35 to 0.40, which was lower than the stoichiometric value for MgMn_2O_4 . Then, the relative concentration of Mg ions continued to increase; the Mg/Mn atomic ratio was ~0.7 to 0.8 at ~5 to 8 nm from the $\text{Mg}_x\text{Mn}_2\text{O}_4/\text{SRO}$ interface and ~1.0 to 1.1 at the top ~2-nm-thick layer. The amorphous layer with high Mg concentration at the film surface indicated that the overall transport during discharge was likely limited by overmagnesiation at the cathode/electrolyte interface and consequential collapse of the spinel structure.

Higher-magnification view of the $\text{Mg}_x\text{Mn}_2\text{O}_4/\text{SRO}$ region, shown in Figure 7a, revealed a more detailed picture of structural transformation during deep discharge. The hetero-interface between $\text{Mg}_x\text{Mn}_2\text{O}_4$ and SRO appeared to be abrupt, while the SRO maintained an epitaxial relationship with the film. The film within the first ~4 to 5 nm (I and II) from the $\text{Mg}_x\text{Mn}_2\text{O}_4/\text{SRO}$ interface maintained the spinel structure after deep discharge (see the Supporting Information for the

chemical composition difference in regions I and II). This was followed by the crystalline layer (III), which showed clear changes in the crystal structure, potentially indicating transition to the disordered rock-salt-type structure due to overmagnesiation³⁶ as the EDS points to ~0.7 to 0.8 of the Mg/Mn atomic ratio. Lastly, an amorphous top layer (IV) was found. The electron energy-loss spectroscopy (EELS) spectra taken from these four distinct regions are shown in Figure 7b, specifically with the O K- and Mn L-edge fine structures, located around 530 and 642 eV, respectively. Albeit noisy, the O K-edge fine structure in the I and II regions exhibited the features associated with a spinel structure.³⁷ We labeled two prominent features in the near-edge fine structure of the K-edge, as shown in Figure 7b. In the III and IV regions, the O K-edge onset shifted toward higher energy, indicating decreasing Mn valence,³⁸ and most of the near-edge fine-structure peaks, such as peaks a and b, vanished at the top surface of the film. The lack of the near-edge fine structure in the K-edge is associated with the loss of the long-range crystal order, thus confirming its amorphization. On the other hand, the energy of the L-edges of manganese can be used to assess its valence state.³⁹ In agreement with the EDS data shown in Figure 6b, the Mn L-edge onset energy decreased as moving toward the top surface of the $\text{Mg}_x\text{Mn}_2\text{O}_4$ film from the I to the IV region, indicating that manganese was reduced as the Mg concentration increased (magnified view of the Mn L-edges is provided in Figure S4). Moreover, the Mn L-edge signal intensity, a direct measure of the local concentration of Mn, continued to decrease and became the lowest in the IV region, implying potential presence of Mg-rich phases like MgMn_2O_4 in the amorphous top layer (possibly a mixture of MgO and MnO).^{12,16,40}

A closer look into the shift in the 111 *d*-spacing with time (Figure 5g), on the other hand, revealed that the rate of lattice change was much faster for magnesium insertion than for extraction, and the overall lattice constant tended to creep higher for each cycle. This suggested that Mg insertion was more favorable than extraction, even in a 10-nm-thick film. Consistent with this analysis, charged cathode films (i.e., $\lambda\text{-Mn}_2\text{O}_4$) were surprisingly prone to self-discharge under the nonaqueous electrolyte system used in this study (see Figure S5 and texts). This observation was somewhat contradictory to

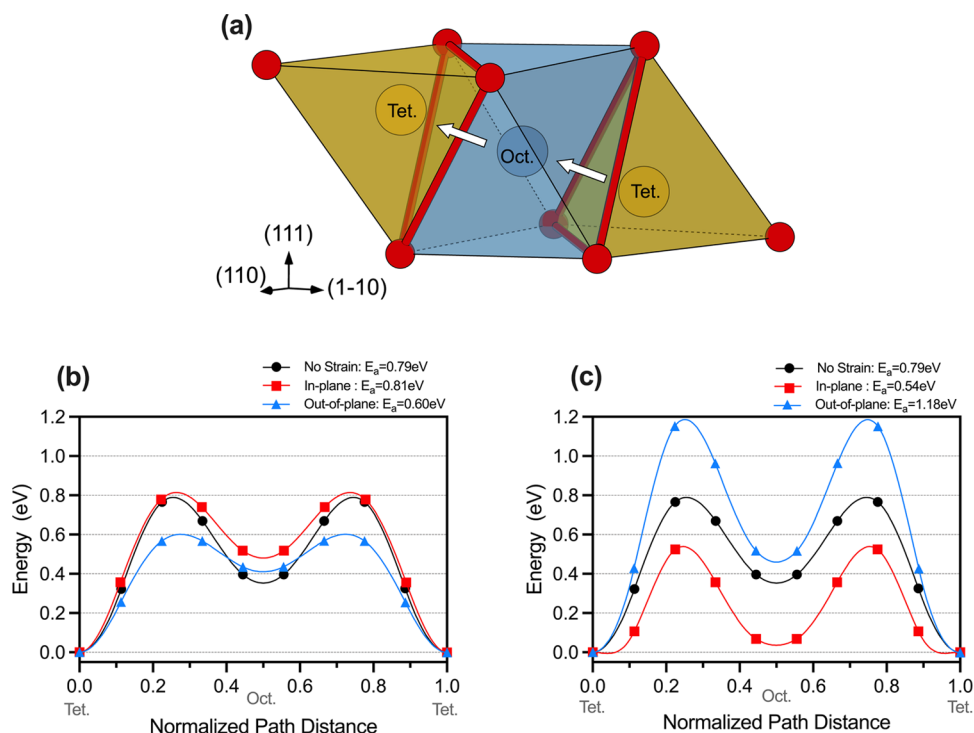


Figure 8. (a) Schematic path of Mg^{2+} diffusion between two adjacent tetrahedral (Tet.) sites through the octahedral site (Oct.). DFT-calculated energies for Mg^{2+} diffusion along the minimal energy path connecting two tetrahedral sites in the case of (b) 5% biaxial tensile strain normal to the (111) plane and (c) 5% biaxial compressive strain. In both cases, the minimum energy path for the case of no strain is provided for comparison.

computational expectation¹⁴ and experimental observation during chemical deintercalation in an aqueous electrolyte.²⁸ Different transport kinetics during Mg-ion insertion and extraction could be associated with strain developed in a film. The initial (111) *d*-spacing of the as-deposited film indicated that the film was relaxed to its bulk lattice constant during growth, instead of adopting the much smaller in-plane substrate lattice constant. However, in-plane strain can be introduced during charge and discharge since the film constrained by a substrate cannot expand or contract laterally to accommodate volume changes upon Mg insertion or extraction, respectively.^{41,42} As a result, in its charged state (contracted film volume), the spinel film can be in tensile biaxial strain, whereas the Mg-rich discharged sample (increased film volume) can be compressed in-plane.

Strain-driven modification of Mg-ion transport kinetics was investigated by calculating Mg-ion migration barriers in a high Mg vacancy limit in a biaxially strained $\text{Mg}_x\text{Mn}_2\text{O}_4$ spinel, using DFT calculations. In a spinel structure, Mg diffusion proceeds from a tetrahedral site through the neighboring face-sharing octahedral site so that the diffusion barrier occurs at the faces of equilateral triangles shared by tetrahedra and octahedra, as shown in Figure 8a. Here, biaxial strain can cause asymmetric distortion of triangles depending on crystallographic directions and, ultimately, modify diffusion barriers through the in-plane and out-of-plane directions in a different way. Here, applied strain for the in-plane directions was defined relative to LMO lattice parameters ($a = b = 8.15\text{ \AA}$), while the lattice parameter in the out-of-plane [111] direction was determined by geometry optimization. Figure 8b,c compares Mg-ion diffusion barriers, calculated for no strain case with 5% biaxial tensile and compressive strains, respectively. The 5% strain was chosen because the lattice parameter variation upon (de)intercalation of MgMn_2O_4 , as

calculated by DFT, is of similar magnitude. Previous calculations found ~600 to 800 meV of Mg-ion migration barriers in an unstrained bulk spinel,¹⁴ which was consistent with our energy barrier result of 790 meV. In the case of tensile strain (Figure 8b), which represented the charged state (i.e., $\lambda\text{-Mn}_2\text{O}_4$), the out-of-plane Mg-ion movement showed smaller activation energy (600 meV of diffusion barrier), compared to the in-plane movement (810 meV) and the strain-free case, implying facile out-of-plane Mg insertion at initial discharge. In contrast, under compressive strain (Figure 8c), which could occur both in the middle of discharge and during subsequent charge, out-of-plane Mg-ion movement is needed to overcome higher activation energy (1180 meV). This suggested that further Mg transport through the film can be impeded, leading to Mg surface enrichment and sluggish Mg extraction. Interestingly, the activation energy for in-plane migration under compressive strain decreased from 790 to 540 meV, and the energy difference between a tetrahedral site and an octahedral site became considerably reduced, suggesting a possibility of a higher degree of inversion and spinel-to-rock-salt transition. Additional calculations for the relaxed and biaxially strained MgMn_2O_4 phase indicated that the formation of the overmagnesiated surface layer could arrest further Mg transport along both out-of-plane and in-plane directions (see Figures S6 and S7 and texts). Specifically, the energy barriers were above 1500 meV for compressive strain and depended strongly on the magnitudes of biaxial strain applied along [110] and [11̄2] to mimic the [111] growth direction. For instance, the energy barriers decreased to 600 meV under +5% tensile strain, indicating that maintaining high tensile strain in overmagnesiated surface layers might be beneficial for Mg transport. For the structure stained along [100] and [010] to mimic the [001] growth direction, the energy barriers varied from 1600 to 1900 meV and depended weakly on the

magnitudes of biaxial strain, indicating much lower in-plane Mg mobility in overmagnesiated layers.

CONCLUSIONS

This study builds on a growing number of literature showing that magnesium-based spinel oxides are susceptible to surface Mg enrichment forming a rock-salt-like surface layer, which could impede Mg transport. Here, we investigated how the insertion and extraction of magnesium ion evolved near the surface of the manganese-based spinel structure in real-time by using X-ray scattering, combining with post-mortem microscopy observation and insight from the DFT calculation. We found that an initial Mg insertion to the empty spinel ($\lambda\text{-Mn}_2\text{O}_4$) occurred at expected potentials (3–4 V), but both X-ray scattering and TEM analysis indicated that the surface of the $\text{Mg}_x\text{Mn}_2\text{O}_4$ film tended to be overmagnesiated, eventually leading to amorphization. On the other hand, subsequent charge process appeared to be slower and limited, and complete Mg extraction may require higher voltages that are beyond the anodic stability of this electrolyte. Previous bulk studies have shown significant hysteresis between discharge and charge, which may indicate such an overpotential.^{19,28} The surface Mg enrichment and high overpotential are likely related to the diffusion barriers near the surface, calculated by DFT, which could depend on strain evolved from the film volume change constrained by the substrate during Mg insertion and extraction. Particularly, in the compressive strain case for subsequent Mg extraction, in-plane migration is strongly favored over out-of-plane diffusion, creating a substantial kinetic barrier for the transport of Mg through the film surface. While this situation may be only related to the unique strain conditions of a thin film, it is worth noting that even in a 3D crystallite, a rock-salt surface layer would have a similar compressive strain with respect to the underlying crystal structure of the spinel. The present results demonstrated that irreversible Mg transport at the electrode–electrolyte interface could be a limiting factor for practical use of a spinel cathode, and strain induced by volume and phase change needs to be considered. In that sense, rational design of spinel toward less volume change, cubic phase stabilized by solid solution (e.g., MgCrMnO_4), and reversible transition between spinel and rock-salt phases during Mg insertion/extraction could be a promising approach.^{19,43}

ASSOCIATED CONTENT

Supporting Information

The Supporting Information is available free of charge at <https://pubs.acs.org/doi/10.1021/acs.chemmater.3c02490>.

Modeled 111 film Bragg peak intensity and position upon Li extraction and Mg insertion; current density profile during CV measurements for the second sample; TEM on interfaces between STO, SRO, and LMO films; magnified view of the Mn L-edges; Mg/Mn ratio obtained from EDS; self-discharge of the $\lambda\text{-Mn}_2\text{O}_4$ film; and impact of lateral strain and crystallographic orientation on Mg transport in MgMnO_2 ([PDF](#))

AUTHOR INFORMATION

Corresponding Authors

Jae Jin Kim – Chemical Sciences and Engineering Division and Joint Center for Energy Storage Research (JCESR), Argonne National Laboratory, Lemont, Illinois 60439, United States;

 orcid.org/0000-0001-7709-3530; Email: jaekim@anl.gov

Timothy T. Fister – Chemical Sciences and Engineering Division and Joint Center for Energy Storage Research (JCESR), Argonne National Laboratory, Lemont, Illinois 60439, United States;  orcid.org/0000-0001-6537-6170; Email: fister@anl.gov

Authors

Bilash KC – Department of Physics, University of Illinois – Chicago, Chicago, Illinois 60607, United States

Haesun Park – School of Integrative Engineering, Chung-Ang University, Seoul 06974, Republic of Korea;  orcid.org/0000-0001-6266-8151

Aditya Sundar – Joint Center for Energy Storage Research (JCESR) and Materials Science Division, Argonne National Laboratory, Lemont, Illinois 60439, United States

Guennadi Evmenenko – Materials Science and Engineering Department, Northwestern University, Evanston, Illinois 60208, United States;  orcid.org/0000-0002-6580-2237

D. Bruce Buchholz – Materials Science and Engineering Department, Northwestern University, Evanston, Illinois 60208, United States

Jinglong Guo – Department of Physics, University of Illinois – Chicago, Chicago, Illinois 60607, United States

Brian J. Ingram – Chemical Sciences and Engineering Division and Joint Center for Energy Storage Research (JCESR), Argonne National Laboratory, Lemont, Illinois 60439, United States;  orcid.org/0000-0002-5219-7517

Peter Zapol – Joint Center for Energy Storage Research (JCESR) and Materials Science Division, Argonne National Laboratory, Lemont, Illinois 60439, United States;  orcid.org/0000-0003-0570-9169

Robert F. Klie – Department of Physics, University of Illinois – Chicago, Chicago, Illinois 60607, United States;  orcid.org/0000-0003-4773-6667

Complete contact information is available at:

<https://pubs.acs.org/10.1021/acs.chemmater.3c02490>

Notes

The authors declare no competing financial interest.

ACKNOWLEDGMENTS

This work was primarily supported and intellectually led by the Joint Center for Energy Storage Research (JCESR) and the Energy Innovation Hub funded by the U.S. Department of Energy (DOE), Office of Science, and Basic Energy Sciences. Thin-film growth at the Pulsed Laser Deposition Shared Facility, Materials Research Center at Northwestern University, was supported by the National Science Foundation MRSEC Program (DMR-2308691) and the Soft and Hybrid Nanotechnology Experimental (SHyNE) Resource (NSF ECCS-2025633). This work made use of the Jerome B. Cohen X-ray Diffraction Facility supported by the MRSEC program of the National Science Foundation (DMR-2308691) at the Materials Research Center of Northwestern University and the Soft and Hybrid Nanotechnology Experimental (SHyNE) Resource (NSF ECCS-1542205). This work made use of instruments in the Electron Microscopy Service, specifically JEOL JEM-ARM200CF in the Research Resources Center, University of Illinois at Chicago. The acquisition of UIC JEOL JEM-ARM200CF was supported by an MRI-R2 Grant from the National Science Foundation (DMR-

0959470), and the upgraded Gatan Continuum spectrometer was supported by a grant from the NSF (DMR-1626065). The authors acknowledge the computing resources provided on Bebop, a high-performance computing cluster operated by the Laboratory Computing Resource Center at Argonne National Laboratory. Use of the Advanced Photon Source at Argonne National Laboratory was supported by the U.S. Department of Energy, Office of Science, Office of Basic Energy Sciences, under Contract No. DE-AC02-06CH11357.

■ REFERENCES

- (1) Yoo, H. D.; Shterenberg, I.; Gofer, Y.; Gershinsky, G.; Pour, N.; Aurbach, D. Mg rechargeable batteries: an on-going challenge. *Energy Environ. Sci.* **2013**, *6* (8), 2265–2279.
- (2) Ponorouch, A.; Frontera, C.; Bardé, F.; Palacín, M. R. Towards a calcium-based rechargeable battery. *Nat. Mater.* **2016**, *15* (2), 169–172.
- (3) Wang, M.; Jiang, C.; Zhang, S.; Song, X.; Tang, Y.; Cheng, H.-M. Reversible calcium alloying enables a practical room-temperature rechargeable calcium-ion battery with a high discharge voltage. *Nat. Chem.* **2018**, *10* (6), 667–672.
- (4) Shyamsunder, A.; Blanc, L. E.; Assoud, A.; Nazar, L. F. Reversible Calcium Plating and Stripping at Room Temperature Using a Borate Salt. *ACS Energy Lett.* **2019**, *4* (9), 2271–2276.
- (5) Aurbach, D.; Lu, Z.; Schechter, A.; Gofer, Y.; Gizbar, H.; Turgeman, R.; Cohen, Y.; Moshkovich, M.; Levi, E. Prototype systems for rechargeable magnesium batteries. *Nature* **2000**, *407* (6805), 724–727.
- (6) Mitelman, A.; Levi, M. D.; Lancry, E.; Levi, E.; Aurbach, D. New cathode materials for rechargeable Mg batteries: fast Mg ion transport and reversible copper extrusion in Cu_yMo₆S₈ compounds. *Chem. Commun.* **2007**, No. 41, 4212–4214.
- (7) Sun, X.; Bonnick, P.; Nazar, L. F. Layered TiS₂ Positive Electrode for Mg Batteries. *ACS Energy Lett.* **2016**, *1* (1), 297–301.
- (8) Bonnick, P.; Blanc, L.; Vajargah, S. H.; Lee, C.-W.; Sun, X.; Balasubramanian, M.; Nazar, L. F. Insights into Mg²⁺ Intercalation in a Zero-Strain Material: Thiospinel Mg_xZr₂S₄. *Chem. Mater.* **2018**, *30* (14), 4683–4693.
- (9) Muldoon, J.; Bucur, C. B.; Gregory, T. Quest for Nonaqueous Multivalent Secondary Batteries: Magnesium and Beyond. *Chem. Rev.* **2014**, *114* (23), 11683–11720.
- (10) Lipson, A. L.; Han, S.-D.; Pan, B.; See, K. A.; Gewirth, A. A.; Liao, C.; Vaughey, J. T.; Ingram, B. J. Practical Stability Limits of Magnesium Electrolytes. *J. Electrochem. Soc.* **2016**, *163* (10), A2253–A2257.
- (11) Huie, M. M.; Bock, D. C.; Takeuchi, E. S.; Marschilok, A. C.; Takeuchi, K. J. Cathode materials for magnesium and magnesium-ion based batteries. *Coord. Chem. Rev.* **2015**, *287*, 15–27.
- (12) Canepa, P.; Sai Gautam, G.; Hannah, D. C.; Malik, R.; Liu, M.; Gallagher, K. G.; Persson, K. A.; Ceder, G. Odyssey of Multivalent Cathode Materials: Open Questions and Future Challenges. *Chem. Rev.* **2017**, *117* (5), 4287–4341.
- (13) Mao, M.; Gao, T.; Hou, S.; Wang, C. A critical review of cathodes for rechargeable Mg batteries. *Chem. Soc. Rev.* **2018**, *47* (23), 8804–8841.
- (14) Liu, M.; Rong, Z.; Malik, R.; Canepa, P.; Jain, A.; Ceder, G.; Persson, K. A. Spinel compounds as multivalent battery cathodes: a systematic evaluation based on ab initio calculations. *Energy Environ. Sci.* **2015**, *8* (3), 964–974.
- (15) Bayliss, R. D.; Key, B.; Sai Gautam, G.; Canepa, P.; Kwon, B. J.; Lapidus, S. H.; Dogan, F.; Adil, A. A.; Lipton, A. S.; Baker, P. J.; Ceder, G.; Vaughey, J. T.; Cabana, J. Probing Mg Migration in Spinel Oxides. *Chem. Mater.* **2020**, *32* (2), 663–670.
- (16) Sa, N.; Mukherjee, A.; Han, B.; Ren, Y.; Klie, R. F.; Key, B.; Vaughey, J. T. Direct observation of MgO formation at cathode electrolyte interface of a spinel MgCo₂O₄ cathode upon electrochemical Mg removal and insertion. *J. Power Sources* **2019**, *424*, 68–75.
- (17) Okamoto, S.; Ichitsubo, T.; Kawaguchi, T.; Kumagai, Y.; Oba, F.; Yagi, S.; Shimokawa, K.; Goto, N.; Doi, T.; Matsubara, E. Intercalation and Push-Out Process with Spinel-to-Rocksalt Transition on Mg Insertion into Spinel Oxides in Magnesium Batteries. *Adv. Sci.* **2015**, *2* (8), No. 1500072.
- (18) Truong, Q. D.; Kempaiah Devaraju, M.; Tran, P. D.; Gambe, Y.; Nayuki, K.; Sasaki, Y.; Honma, I. Unravelling the Surface Structure of MgMn₂O₄ Cathode Materials for Rechargeable Magnesium-Ion Battery. *Chem. Mater.* **2017**, *29* (15), 6245–6251.
- (19) Kwon, B. J.; Yin, L.; Park, H.; Parajuli, P.; Kumar, K.; Kim, S.; Yang, M.; Murphy, M.; Zapol, P.; Liao, C.; Fister, T. T.; Klie, R. F.; Cabana, J.; Vaughey, J. T.; Lapidus, S. H.; Key, B. High Voltage Mg-Ion Battery Cathode via a Solid Solution Cr–Mn Spinel Oxide. *Chem. Mater.* **2020**, *32* (15), 6577–6587.
- (20) Yin, L.; Kwon, B. J.; Choi, Y.; Bartel, C. J.; Yang, M.; Liao, C.; Key, B.; Ceder, G.; Lapidus, S. H. Operando X-ray Diffraction Studies of the Mg-Ion Migration Mechanisms in Spinel Cathodes for Rechargeable Mg-Ion Batteries. *J. Am. Chem. Soc.* **2021**, *143* (28), 10649–10658.
- (21) Feng, Z.; Chen, X.; Qiao, L.; Lipson, A. L.; Fister, T. T.; Zeng, L.; Kim, C.; Yi, T.; Sa, N.; Proffit, D. L.; Burrell, A. K.; Cabana, J.; Ingram, B. J.; Biegalski, M. D.; Bedzyk, M. J.; Fenter, P. Phase-Controlled Electrochemical Activity of Epitaxial Mg-Spinel Thin Films. *ACS Appl. Mater. Interfaces* **2015**, *7* (51), 28438–28443.
- (22) Evmenenko, G.; Warburton, R. E.; Yildirim, H.; Greeley, J. P.; Chan, M. K. Y.; Buchholz, D. B.; Fenter, P.; Bedzyk, M. J.; Fister, T. T. Understanding the Role of Overpotentials in Lithium Ion Conversion Reactions: Visualizing the Interface. *ACS Nano* **2019**, *13* (7), 7825–7832.
- (23) Thackeray, M. M.; David, W. I. F.; Bruce, P. G.; Goodenough, J. B. Lithium insertion into manganese spinels. *Mater. Res. Bull.* **1983**, *18* (4), 461–472.
- (24) Thackeray, M. M. Manganese oxides for lithium batteries. *Prog. Solid State Chem.* **1997**, *25* (1), 1–71.
- (25) Chen, X.; Vörös, M.; Garcia, J. C.; Fister, T. T.; Buchholz, D. B.; Franklin, J.; Du, Y.; Droubay, T. C.; Feng, Z.; Iddir, H.; Curtiss, L. A.; Bedzyk, M. J.; Fenter, P. Strain-Driven Mn-Reorganization in Overlithiated Li_xMn₂O₄ Epitaxial Thin-Film Electrodes. *ACS Appl. Energy Mater.* **2018**, *1* (6), 2526–2535.
- (26) Torres-Castanedo, C. G.; Evmenenko, G.; Luu, N. S.; Das, P. M.; Hyun, W. J.; Park, K.-Y.; Dravid, V. P.; Hersam, M. C.; Bedzyk, M. J. Enhanced LiMn₂O₄ Thin-Film Electrode Stability in Ionic Liquid Electrolyte: A Pathway to Suppress Mn Dissolution. *ACS Appl. Mater. Interfaces* **2023**, *15* (29), 35664–35673.
- (27) Lau, K.-C.; Seguin, T. J.; Carino, E. V.; Hahn, N. T.; Connell, J. G.; Ingram, B. J.; Persson, K. A.; Zavadil, K. R.; Liao, C. Widening Electrochemical Window of Mg Salt by Weakly Coordinating Perfluoroalkoxyaluminate Anion for Mg Battery Electrolyte. *J. Electrochem. Soc.* **2019**, *166* (8), A1510–A1519.
- (28) Kim, C.; Phillips, P. J.; Key, B.; Yi, T.; Nordlund, D.; Yu, Y.-S.; Bayliss, R. D.; Han, S.-D.; He, M.; Zhang, Z.; Burrell, A. K.; Klie, R. F.; Cabana, J. Direct Observation of Reversible Magnesium Ion Intercalation into a Spinel Oxide Host. *Adv. Mater.* **2015**, *27* (22), 3377–3384.
- (29) Hohenberg, P.; Kohn, W. Inhomogeneous Electron Gas. *Phys. Rev.* **1964**, *136* (3B), B864–B871.
- (30) Kresse, G.; Furthmüller, J. Efficient iterative schemes for ab initio total-energy calculations using a plane-wave basis set. *Phys. Rev. B* **1996**, *54* (16), 11169–11186.
- (31) Henkelman, G.; Überuaga, B. P.; Jónsson, H. A climbing image nudged elastic band method for finding saddle points and minimum energy paths. *J. Chem. Phys.* **2000**, *113* (22), 9901–9904.
- (32) Blöchl, P. E. Projector augmented-wave method. *Phys. Rev. B* **1994**, *50* (24), 17953–17979.
- (33) Kresse, G.; Joubert, D. From ultrasoft pseudopotentials to the projector augmented-wave method. *Phys. Rev. B* **1999**, *59* (3), 1758–1775.

- (34) Perdew, J. P.; Burke, K.; Ernzerhof, M. Generalized Gradient Approximation Made Simple. *Phys. Rev. Lett.* **1996**, *77* (18), 3865–3868.
- (35) Greedan, J. E.; Raju, N. P.; Wills, A. S.; Morin, C.; Shaw, S. M.; Reimers, J. N. Structure and Magnetism in λ -MnO₂. Geometric Frustration in a Defect Spinel. *Chem. Mater.* **1998**, *10* (10), 3058–3067.
- (36) Hatakeyama, T.; Okamoto, N. L.; Shimokawa, K.; Li, H.; Nakao, A.; Uchimoto, Y.; Tanimura, H.; Kawaguchi, T.; Ichitsubo, T. Electrochemical phase transformation accompanied with Mg extraction and insertion in a spinel MgMn₂O₄ cathode material. *Phys. Chem. Chem. Phys.* **2019**, *21* (42), 23749–23757.
- (37) Phillips, P. J.; Iddir, H.; Abraham, D. P.; Klie, R. F. Direct observation of the structural and electronic changes of Li₂MnO₃ during electron irradiation. *Appl. Phys. Lett.* **2014**, *105* (11), No. 113905.
- (38) Tan, H.; Verbeeck, J.; Abakumov, A.; Van Tendeloo, G. Oxidation state and chemical shift investigation in transition metal oxides by EELS. *Ultramicroscopy* **2012**, *116*, 24–33.
- (39) Gao, X.; Ikuhara, Y. H.; Fisher, C. A. J.; Moriwake, H.; Kuwabara, A.; Oki, H.; Kohama, K.; Yoshida, R.; Huang, R.; Ikuhara, Y. Structural Distortion and Compositional Gradients Adjacent to Epitaxial LiMn₂O₄ Thin Film Interfaces. *Adv. Mater. Interfaces* **2014**, *1* (8), No. 1400143.
- (40) Hannah, D. C.; Sai Gautam, G.; Canepa, P.; Ceder, G. On the Balance of Intercalation and Conversion Reactions in Battery Cathodes. *Adv. Energy Mater.* **2018**, *8* (20), No. 1800379.
- (41) Zoo, Y.; Adams, D.; Mayer, J. W.; Alford, T. L. Investigation of coefficient of thermal expansion of silver thin film on different substrates using X-ray diffraction. *Thin Solid Films* **2006**, *513* (1), 170–174.
- (42) Liu, M. Finite element analysis of lithium insertion-induced expansion of a silicon thin film on a rigid substrate under potentiostatic operation. *J. Power Sources* **2015**, *275*, 760–768.
- (43) Shimokawa, K.; Atsumi, T.; Harada, M.; Ward, R. E.; Nakayama, M.; Kumagai, Y.; Oba, F.; Okamoto, N. L.; Kanamura, K.; Ichitsubo, T. Zinc-based spinel cathode materials for magnesium rechargeable batteries: toward the reversible spinel–rocksalt transition. *J. Mater. Chem. A* **2019**, *7* (19), 12225–12235.